A Prokaryotic Membrane Sculpting BAR Domain Protein

Daniel A. Phillips[1*], Lori A. Zacharoff[2*], Cheri M. Hampton[3], Grace W. Chong[4], Anthony P. Malanoski[5], Lauren Ann Metskas[6], Shuai Xu[2], Lina J. Bird[5], Brian J. Eddie[5], Grant J. Jensen[6,7], Lawrence F. Drummy[3], Mohamed Y. El-Naggar[2,4,8], and Sarah M. Glaven[5]

[1]American Society for Engineering Education, Washington, DC, USA.
[2]University of Southern California, Department of Physics and Astronomy, Los Angeles, CA 90089
[3]Materials and Manufacturing Directorate, Air Force Research Laboratory, Wright-Patterson Air Force Base, WPAFB, OH, USA.
[4]University of Southern California, Department of Biological Sciences, Los Angeles, CA 90089
[5]Center for Bio/Molecular Science and Engineering, Naval Research Laboratory, Washington, DC, USA.
[6]California Institute of Technology, Division of Biology and Biological Engineering, Pasadena, CA 91125
[7]California Institute of Technology, Howard Hughes Medical Institute, Pasadena, CA 91125
[8]University of Southern California, Department of Chemistry, Los Angeles, CA 90089

[*]These authors contributed equally to this work

Classification: Biological sciences

Keywords: BAR domain | extracellular electron transport | membrane shaping | outer membrane vesicles | outer membrane extensions | *Shewanella*

Send all correspondence to:
Daniel A. Phillips
Daniel.phillips.ctr@nrl.navy.mil
(423) 215-2256
4555 Overlook Ave.
Washington, DC 20375

Lori A. Zacharoff
zacharof@usc.edu
(763) 221-0960
920 Bloom Walk
SSC, 215C
Los Angeles, CA 90089

Abstract

Bin/Amphiphysin/RVS (BAR) domain proteins belong to a superfamily of coiled-coil proteins that influence membrane curvature in eukaryotes and are associated with vesicle biogenesis, vesicle-mediated protein trafficking, and intracellular signaling(1-6). BAR domain proteins have not been identified in bacteria, despite certain organisms displaying an array of membrane curvature phenotypes(7-16). Here we identify a prokaryotic BAR domain protein, BdpA, from *Shewanella oneidensis* MR-1, an iron reducing bacterium known to produce redox active membrane vesicles and micrometer-scale membrane extensions. BdpA is required for uniform size distribution of outer membrane vesicles and is responsible for scaffolding outer membrane extensions (OMEs) into membrane structures with consistent diameter and curvature. While a strain lacking BdpA produces OMEs, cryogenic transmission electron microscopy reveals more lobed, disordered OMEs rather than the membrane tubes produced by the wild type strain. Overexpression of BdpA promotes OME formation even during planktonic conditions where *S. oneidensis* OMEs are less common. Heterologous expression also results in OME production in *Marinobacter atlanticus* CP1 and *Escherichia coli*. Based on the ability of BdpA to alter membrane curvature *in vivo*, we propose that BdpA and its homologs comprise a newly identified class of prokaryotic BAR (P-BAR) domains that will aid in identification of putative P-BAR proteins in other bacterial species.

21 **Significance Statement:**

22 BAR domain proteins are a crucial component of membrane architecture and
23 vesicle trafficking in eukaryotic cells. Despite the recognized importance of BAR domain
24 proteins in eukaryotic cell biology, this family of proteins has never before been reported
25 for prokaryotes. Previously, outer membrane extensions of *Shewanella oneidensis* were
26 shown to transition between chains of vesicles and tubules. We identified a component
27 critical to structural transition as the first BAR domain protein in prokaryotes, which we
28 term BdpA (BAR domain-like protein A). We show that BdpA (i) is enriched in outer
29 membrane structures; (ii) is critical to regulate size of outer membrane vesicles; (iii)
30 controls the shape of outer membrane extensions; (iv) confers membrane extension
31 formation capabilities when expressed in other bacteria.

32

33 **Main**

34 Eukaryotic Bin/Amphiphysin/Rvs (BAR) domain-containing proteins generate
35 membrane curvature through electrostatic interactions between positively charged amino
36 acids and negatively charged lipids, scaffolding the membrane along the intrinsically
37 curved surface of the antiparallel coiled-coil protein dimers(17-20). Some BAR domain-
38 containing proteins, such as the N-BAR protein BIN1, contain amphipathic helical wedges
39 that insert into the outer membrane leaflet and can assist in membrane binding(21). Other
40 BAR domains can be accompanied by a membrane targeting domain, such as PX for
41 phosphoinositide binding(22, 23), in order to direct membrane curvature formation at
42 specific sites, as is the case with sorting nexin BAR proteins(4). The extent of
43 accumulation of BAR domain proteins at a specific site can influence the degree of the

44 resultant membrane curvature(24), and tubulation events arise as a consequence of BAR
45 domain multimerization in conjunction with lipid binding(25). Interactions between BAR
46 domain proteins and membranes resolve membrane tension, promote membrane
47 stability, and aid in localizing cellular processes, such as actin binding, signaling through
48 small GTPases, membrane vesicle scission, and vesicular transport of proteins(1, 26,
49 27). Despite our knowledge of numerous eukaryotic BAR proteins spanning a variety of
50 modes of curvature formation, membrane localizations, and subtypes (N-BAR, F-BAR,
51 and I-BAR), characterization of a functional prokaryotic BAR domain protein has yet to be
52 reported.

53 Bacterial cell membrane curvature can be observed during the formation of outer
54 membrane vesicles (OMV) and outer membrane extensions (OME). OMV formation is
55 ubiquitous and has many documented functions(9). OMEs are less commonly observed,
56 remain attached to the cell, and various morphologies can be seen extending from single
57 cells including *Myxococcus xanthus*(14, 15), flavobacterium strain Hel3_A1_48(8), *Vibrio*
58 *vulnificus*(10), *Francisella novicida*(28), *Shewanella oneidensis*(7, 29-31), and as cell-cell
59 connections in *Bacillus subtilis*(32-34) and *Eschericia coli*(35). Several bacterial proteins
60 have demonstrated membrane tubule formation capabilities *in vitro*(16, 36-40), but
61 despite the growing number of reports, proteins involved in shaping bacterial membranes
62 into OMV/Es have yet to be identified. Recently, researchers have begun to suspect that
63 OMV and OME formation has some pathway overlap(8), and it is proposed that proteins
64 are necessary to stabilize these structures(13).

65 ***S. oneidensis* OMVs are redox-active and enriched with BdpA**

66 *Shewanella oneidensis* is known to produce redox-active OMVs(41) and OMEs
67 coated with mulitheme cytochromes, particularly upon surface attachment(7, 30, 41).
68 However, little is known about their formation mechanism, control of shape or curvature,
69 and electrochemical properties that influence EET function. OMVs were purified from
70 cells grown in batch cultures to characterize the redox features and unique proteome of
71 *S. oneidensis* OMVs, as well as to identify putative membrane shaping proteins.
72 Cryogenic transmission electron microscopy (cryo-TEM) tomographic reconstruction
73 slices of the purified samples showed uniform OMVs with the characteristic single
74 membrane phenotype and an approximate diameter of 200 nm (Fig. 1a). Previous
75 measurements showed OMVs can reduce extracellular electron acceptors(41) and that
76 vesicles from *G. sulfurreducens* can mediate electron transfer(42). Electrochemical
77 activity of multiheme cytochrome complex MtrCAB and their ability to mediate
78 micrometer-scale electron transport has been characterized in whole cells(43), but no
79 electrochemical characterization of OME/Vs has been reported that link activity to
80 multiheme cytochromes. Here, electrochemical measurements of isolated OMVs were
81 performed to determine if purified OMVs maintain the characteristic redox features of the
82 MtrCAB complex when detached from cells. Cyclic voltammetry (CV) demonstrated redox
83 activity of isolated membrane vesicles adhered to a gold electrode via self-assembled
84 monolayers (Fig. 1b). The first derivative (Fig. 1b inset) revealed a prominent peak with
85 a midpoint potential of 66 mV and a smaller peak at -25 mV versus a standard hydrogen
86 reference electrode (SHE). This midpoint potential is consistent with the characteristics
87 of multiheme cytochromes such as MtrC/OmcA from previous microbial electrochemical

88 studies(43, 44), suggesting that the extracellular redox molecules of the cellular outer
89 membrane extends to OMVs.

90 The proteome of the OMVs was compared to the proteome of purified outer
91 membranes extracted from whole cells. Using a label-free quantification method(45),
92 significant differences in the ratio of individual proteins in the vesicle to the outer
93 membrane could be computed (log fold change) (Fig 1c). The proteome of the purified
94 OMVs showed 328 proteins were significantly enriched in the vesicles as compared to
95 the outer membrane, and 314 proteins were significantly excluded from the vesicles (Fig.
96 1c, Supplemental table 1). MtrCAB cytochromes were present in the OMVs as well as
97 the outer membrane, supporting redox activity of OMVs observed by CV. Active protein
98 sorting into eukaryotic vesicles is a coordinated process involving protein sorting signal
99 recognition, localized membrane protein recruitment, initiation of membrane curvature
100 induction, and coating nascent vesicles with protein scaffolds(46). Several proteins
101 significantly enriched in the vesicles were identified that could contribute to OMV
102 formation, including the murein transglycosylase, the peptidoglycan degradation enzyme
103 holin, cell division coordinator CpoB, and a highly enriched putative BAR domain-
104 containing protein encoded by the gene at open reading frame SO_1507, hereafter
105 named BAR domain-like protein A (BdpA) (Fig. 1d).

106 Vesicle enrichment of BdpA led us to the hypothesis that BdpA could be involved
107 in membrane shaping of OMVs based on the role of BAR domain proteins in eukaryotes.
108 The C-terminal BAR domain of BdpA is predicted to span an alpha-helical region from AA
109 276-451 (E-value = 2.96e-03); however, since the identification of the protein is based on
110 homology to the eukaryotic BAR domain consensus sequence (cd07307), it is possible

111 that the BAR domain region extends beyond these bounds (Fig. 1d). Coiled coil
112 prediction(47) suggests BdpA exists in an oligomeric state of antiparallel alpha-helical
113 dimers, as is the case for all known BAR domain proteins(18, 48-50). The predicted
114 structure of the BAR domain-containing region generated in i-TASSER(51) shows a 3
115 helix bundle (Supplemental Fig. 1a). When the BdpA BAR domain monomers were
116 aligned to the dimeric structure of the F-BAR protein Hof1p(52), the predicted dimer
117 interface residues of BdpA came into proximity, revealing an intrinsically curved dimer
118 with positively charged residues along the concave surface (Supplemental Fig. 1b). BdpA
119 has a N-terminal signal peptide with predicted cleavage sites between amino acids 22-
120 23, suggesting non-cytoplasmic localization (Fig. 1d). A galactose-binding domain-like
121 region positioned immediately downstream of the signal peptide supports lipid targeting
122 activity seen in other BAR domain proteins, such as the eukaryotic sorting nexins(3) which
123 have phox (PX) domains that bind phosphoinositides(53). The *S. oneidensis* rough-type
124 lipopolysaccharide (LPS) contains 2-acetamido-2-deoxy-D-galactose(54), which
125 suggests possible localization of the protein to the outer leaflet of the outer membrane.

126 **BdpA controls size distribution of vesicles**

127 To determine whether BdpA influences vesicle morphology, OMVs were harvested
128 from wild type (WT) cells and cells in which the gene for BdpA had been deleted (Δ*bdpA*),
129 and their diameters were measured by dynamic light scattering (DLS). WT OMVs had a
130 median diameter of 190 nm with little variability in the population (standard deviation (s.d.)
131 = ±21 nm), while the diameters of Δ*bdpA* OMVs were distributed over a wider range with
132 a median value of 280 nm (s.d. = ± 131 nm (Fig 2a). The data suggest BdpA controls
133 vesicle diameter in membrane structures *ex vivo*, potentially acting by stabilizing OMVs.

134 Cell-associated OMV frequency and size distribution was also measured in live
135 cultures using a perfusion flow imaging platform and the membrane stain FM 4-64, as
136 described previously(29). *S. oneidensis* strains were monitored for OME/V production
137 and progression over the course of 5 hours (>5 fields of view per replicate, n=3) using
138 time-lapse imaging. Spherical membrane stained extracellular structures were classified
139 as OMVs, while larger aspect ratio (i.e. length greater than the width) structures were
140 classified as OMEs. The proportion of cells producing 'large' vesicles, defined as having
141 a membrane clearly delineated from the interior of the vesicles and typically >300 nm,
142 was quantified, and Δ*bdpA* cells produced significantly more large vesicles compared to
143 WT cells (Fig. 2b) even though both the overall frequency of vesiculation and extensions
144 were the same (Fig. 2c). Previous studies showed that OMEs transition between large
145 vesicles and OMEs over time(29). BdpA appears to be involved in this transition in
146 *Shewanella* due to the increased frequency of large vesicles from Δ*bdpA* cells. The
147 median diameter of the OMVs is also the apparent maximum diameter observed in outer
148 membrane extensions(29) suggesting BdpA influences membrane morphologies of both
149 structures.

150 **BdpA constrains membrane extension morphology**

151 The resolution of fluorescence microscopy was insufficient to identify
152 morphological differences between OMEs. Cells were also visualized after deposition
153 onto a glass coverslip instead of a perfusion flow chamber as previously reported(7).
154 BdpA was expressed from a 2,4-diacetylphloroglucinol (DAPG)-inducible promoter(55)
155 (P_{PhlF}-BdpA) in the Δ*bdpA* strain containing the plasmid p452-*bdpA* with 12.5 μM DAPG.
156 After 3 hours post deposition on cover glass, OMEs can be seen extending from WT,

157 Δ*bdpA*, and Δ*bdpA* p452-*bdpA* cells (Fig. 3a, Supplemental Fig. 2, Supplemental videos
158 1-3, 5 fields of view, n=3). Similar to perfusion flow experiments, no statistically significant
159 difference in the overall frequency of OME production was observed between the cells in
160 static cultures.

161 Cryo-TEM was used to assess morphological differences between the OMEs in
162 each of the strains at the ultrastructural level. *S. oneidensis* OMEs from unfixed WT,
163 Δ*bdpA,* and Δ*bdpA* p452-*bdpA* strains were visualized at 90 minutes (Supplemental Fig.
164 3) and 3 hours (Fig. 3a) following cell deposition onto EM grids. By 3 hours post
165 inoculation, images of WT cells consistently show narrow, tubule-like OMEs (p = 0.01,
166 student's t-test) or vesicle chains of symmetric curvature (Fig. 3b,c n=31). The Δ*bdpA*
167 OMEs generally appear as lobed, disordered vesicle chains with irregular curvature (p =
168 0.01, student's t-test), and vesicles can be observed branching laterally from lobes on the
169 extensions (Fig. 3b,c n=13). Nascent WT OMEs from previous studies also exhibited
170 lateral branching of vesicles and lobes, but they exhibited uniform curvature and diameter
171 between lobes and were observed immediately following OME formation(29). Tubules
172 were not observed in any Δ*bdpA* OMEs at 3 hours (Fig. 3d, p = 0.01, student's t-test).
173 OMEs from Δ*bdpA* p452-*bdpA* cells appear as a narrow tubules of a uniform curvature or
174 as ordered vesicle chains (Fig. 3b,c n=3), showing that expression of BdpA from a
175 plasmid rescues the mutant phenotype by constricting and ordering OMEs into narrow
176 tubules and chains (Fig. 3d, p = 0.01, student's t-test). Earlier in OME progression at 90
177 minutes, WT OME phenotypes appeared narrow, tubule-like, and seldom interspersed
178 with lobed regions (Supplemental figure 3a). In Δ*bdpA* OMEs, lobed regions are
179 prevalent with irregular curvature (Supplemental figure 3b). Several narrow Δ*bdpA* p452-

180 *bdpA* OMEs evenly interspersed with slight constriction points or "junction densities" were
181 observed extending from a single cell (Supplemental Fig. 3c).

182 **Expression of BdpA results in OMEs during planktonic growth**

183 *S. oneidensis* OMEs are more commonly observed in surface attached cells than
184 planktonic cells(7, 29). BAR domain proteins can directly promote tubule formation from
185 liposomes *in vitro*(24), so inducing expression of an additional copy of the *bdpA* gene
186 prior to attachment could result in OME formation even during planktonic growth. Growth
187 curves were similar in cultures with the pBBR1-mcs2 empty vector in either of the WT or
188 Δ*bdpA* background strains, but induction of *bdpA* in Δ*bdpA* p452-*bdpA* cells at higher
189 concentrations of 1.25 and 12.5 μM 2,4-diacetylphloroglucinol affected the growth rate
190 (Supplemental figure 4). Planktonic cultures inoculated from overnight cultures were
191 induced with 12.5 μM DAPG for 1 hour, labeled with FM 4-64, and imaged by confocal
192 microscopy. Neither WT (Fig. 4) nor WT with the empty plasmid exposed to 12.5 μM
193 DAPG (not shown) displayed OMEs immediately following deposition onto cover glass.
194 However, 12.5 μM DAPG-induced bdpA expression from p452-*bdpA* in the WT backround
195 strain (WT p452-*bdpA*) displayed OMEs immediately, ranging between 1-7 extensions
196 per cell (Figure 4, Supplemental video 4). The abundance of OMEs suggest that
197 increased *bdpA* expression in planktonic cultures can initiate membrane sculpting into
198 OMEs at the expense of cell division.

199 The ultrastructure of OMEs resulting from expression of *bpdA* from WT p452-*bdpA*
200 cells was examined by cryo-TEM, but in this case samples from planktonic cultures were
201 vitrified on EM grids after induction rather than incubation during induction on the EM
202 grids. By expressing extra copies of *bdpA* in the WT strain during planktonic induction,

203 we predicted that OME morphology would be predominately reliant on curvature
204 formation by BdpA rather than other unidentified structural proteins involved in intrinsic
205 OME formation. OMEs appear as tubule-like segments interspersed with pearled regions
206 proximal to the main cell body (Fig. 4b). OMEs from the MR-1 p452-*bdpA* strain are
207 observed as thin, tubule-like outer membrane vesicle chains, suggesting BdpA
208 involvement in the constriction of the larger outer membrane vesicle chains into longer,
209 tubule-like extensions with more evenly interspersed junction densities. The BdpA OME
210 phenotype more closely resembles membrane tubules formed by the F-BAR protein
211 Pacsin1 from eukaryotic cells, showing a mixture of tubule regions interspersed with
212 pearled segments(56, 57). Orientation and association of Pacsin1 dimers on the
213 membrane surface with one another impacted tubule morphology, and BdpA membrane
214 sculpting could be similar mechanistically.

215 **BdpA-mediated membrane extensions in *Marinobacter atlanticus* CP1 and *E. coli*.**

216 To test the effect of expressing BdpA in an organism with no predicted BAR
217 domain-containing proteins and no apparent OME production, BdpA was expressed in
218 *Marinobacter atlanticus* CP1(58). *Marinobacter* and *Shewanella* are of the same
219 phylogenetic order (*Alteromonadales*) and have been used for heterologous expression
220 of other *S. oneidensis* proteins, such as MtrCAB(59, 60). Upon exposure to DAPG, *M.*
221 *atlanticus* containing the p452-*bdpA* construct (CP1 p452-*bdpA*) forms membrane
222 extensions (Figure 4). OMEs ranged from small membrane blebs to OME tubules
223 extending up to greater than 10 μm in length from the surface of the cell (Supplemental
224 Fig. 5). As noted previously, variation in the tubule phenotypes are commonly seen in
225 tubules from eukaryotic F-BAR proteins(56, 57), showing possible mechanistic overlap of

226 mutable membrane curvature functionalities between these two separate BAR domain
227 proteins.

228 In previous membrane curvature formation experiments with eukaryotic BAR
229 domain proteins, localized BAR domain protein concentrations affected the resultant
230 shape of the membranes, ranging from bulges to tubules and branched, reticular tubule
231 networks at the highest protein densities(61-63). We predicted that expression of BdpA
232 in cells optimized for protein overexpression, such *E. coli* BL21(DE3), would show OMEs
233 resembling BAR protein concentration-dependent structures previously observed from
234 eukaryotic BAR protein experiments *in vitro*. While the uninduced *E. coli* BL21(DE3)
235 p452-*bdpA* cells had uniform, continuous cell membranes similar to those of plasmid-free
236 BL21(DE3) cells under the conditions tested, *E. coli* BL21(DE3) cells containing the p452-
237 *bdpA* vector induced with 12.5 μM DAPG had outer membrane extensions and vesicles
238 (Figure 4). When visualized over time, OMEs progressed towards a network of reticular
239 membrane structures extending from the cell (Fig. 4c). After 30 minutes, additional
240 membrane blebs were observed that developed into elongated OMEs by 60 minutes.
241 Growth of *E. coli* OMEs was coincident with shrinking of the cell body (from initial cell
242 length = 4.5 μm to 3.5 μm at 60 minutes), supporting direct membrane sculpting activity
243 of BdpA.

244 **P-BAR: a new BAR domain subtype**

245 The discovery of a novel, functional BAR domain protein in prokaryotes provokes
246 questions into the evolutionary origin of BAR domains, such as whether the BdpA BAR
247 domain in *S. oneidensis* arose as a result of convergent evolution, a horizontal gene
248 transfer event, or has a last common ancestor across all domains of life. BdpA homologs

249 were identified by PSI-BLAST in other *Gammaproteobacteria*, including most but not all
250 species of *Shewanella*, as well as *Alishewanella*, *Rheinheimera*, and *Cellvibrio*
251 (Supplemental Fig. 6). The current BAR domain Pfam Hidden Markov Model (HMM)
252 prediction analysis identified BAR domain features in only 5 of the 52 prokaryotic
253 homologs despite greater than 90% homology to *S. oneidensis* BdpA. An amino acid
254 alignment of the 52 BdpA homologs was used to generate a maximum likelihood
255 phylogenetic tree showing evolutionary relatedness of BdpA orthologs to the BAR domain
256 prediction sequences (Supplemental Fig. 6). The 5 BdpA orthologs predicted to contain
257 a BAR domain based on the current model were subsequently aligned with representative
258 known BAR proteins from the various BAR domain subtypes (N-BAR, F-BAR, and I-
259 BAR)(64). BdpA and its prokaryotic orthologs cluster separately from the eukaryotic BAR
260 proteins in their own distinct clade (Fig. 5), suggesting that while BdpA contains a
261 functional BAR domain, it represents its own class of BAR domain, hereafter named P-
262 BAR (Prokaryotic BAR). It is possible that the P-BAR domain arose as a result of
263 horizontal gene transfer from a eukaryote due to the prevalence of eukaryotic coiled-coil
264 proteins with predicted homology to BdpA after 2 iterations of PSI-BLAST. However, the
265 branch lengths and low bootstrap values supporting the placement of P-BAR relative to
266 other BAR domain subtypes make it challenging to directly infer the evolutionary history
267 of P-BAR domains. Discovery of other putative P-BAR proteins would help to build this
268 analysis, and if future comparative proteomics analysis of OME/Vs demonstrates
269 overlapping activity of BdpA with preferential cargo loading into OME/Vs, it could hint at
270 the evolutionary origins of vesicle-based protein trafficking. Conservation of BAR domain
271 proteins supports the notion that three-dimensional organization of proteins in lipid

272 structures is as important to prokaryotes as it is eukaryotes, and suggests additional novel
273 P-BAR proteins are waiting to be discovered.

274

275 **Methods**

276 **Bacterial strains, plasmids, and medium** The bacterial strains used in this study can
277 be found in Supplemental Table 1. *S. oneidensis* strains were grown aerobically in Luria
278 Bertani (LB) media at 30˚C with 50 µg/mL kanamycin when maintaining the plasmid. To
279 observe membrane extensions, cells were centrifuged and resuspended in a defined
280 media comprised of 30 mM Pipes, 60 mM sodium DL-lactate as an electron donor, 28mM
281 NH_4Cl, 1.34 mM KCl, 4.35 mM NaH_2PO_4, 7.5 mM NaOH, 30 mM NaCl, 1mM $MgCl_2$, 1
282 mM $CaCl_2$, and 0.05 mM ferric nitrilotriacetic acid(30). *Marinobacter atlanticus* CP1
283 strains were grown in BB media (50% LB media, 50% Marine broth) at 30˚C with 100
284 µg/mL kanamycin to maintain the plasmids as described previously(58).

285 Inducible BdpA expression plasmids were constructed for use in *S. oneidensis*
286 MR-1, *M. atlanticus* CP1, and *E. coli* BL21(DE3) using the pBBR1-mcs2 backbone
287 described previously(58). The Marionette sensor components (*phlF* promoter,
288 consitutively expressed PhlF repressor, and yellow fluorescence protein (YFP)) cassette
289 from pAJM.452(55) was cloned into the pBBR1-mcs2 backbone, and the YFP cassette
290 was replaced with the gene encoding BdpA by Gibson assembly (primers in
291 Supplemental Table 2). The resulting plasmid was given the name p452-*bdpA*. The
292 Gibson assembly reactions were electroporated into *E. coli* Top10 DH5α cells
293 (Invitrogen), and the sequences were confirmed through Sanger sequencing (Eurofins
294 genomics). Plasmid constructs were chemically transformed into conjugation-competent

295 *E. coli* WM3064 cells for conjugative transfer into the recipient bacterial strains of *S.*
296 *oneidensis* MR-1 and *M. atlanticus* CP1. The same BdpA expression vector was
297 transformed into *E. coli* BL21(DE3) cells (Invitrogen) by chemical transformation.

298 Generation of a scarless *ΔbdpA* knockout mutant of *S. oneidensis* was performed
299 by combining 1 kilobase fragments flanking upstream and downstream from *bdpA* by
300 Gibson assembly into the pSMV3 suicide vector. The resultant plasmid pSMV3_1507KO
301 was transformed into *E. coli* DH5α λ*pir* strain UQ950 cells for propagation. Plasmid
302 sequences were confirmed by Sanger sequencing before chemical transformation into *E.*
303 *coli* WM3064 for conjugation into *S. oneidensis*. Conjugation of pSMV3_1507KO into *S.*
304 *oneidensis* MR-1 was performed as described previously(31). Optical densities at 600nm
305 were measured to determine growth curves for each strain in either LB or SDM with 50
306 μg/mL kanamycin and 2,4-diacetylphloroglucinol (DAPG) as indicated. Cultures of 500
307 μL samples diluted to an initial OD_{600} of 0.1 were grown in Costar® polystyrene 48 well
308 plates (Corning Incorporated) within a Tecan Infinite M1000 Pro (Grödig, Austria) plate
309 reader at 30°C with shaking agitation at 258 rpm. Optical densities were recorded every
310 15 minutes with i-Control software (2.7). All measurements were performed in triplicate.

311 **Purification of Outer Membrane Vesicles** *S. oneidensis* MR-1 cells were grown in LB
312 in 1L non-baffled flasks at 30° C at 200 RPM. When an OD_{600} of 3.0 was reached, cells
313 were pelleted by centrifugation at 5000 x g for 20 min at 4°C, resulting supernatant was
314 filtered through a 0.45 μm filter to remove remaining bacterial cells. Vesicles were
315 obtained by centrifugation at 38,400 x g for 1 h at 4°C in an Avanti J-20XP centrifuge
316 (Beckman Coulter, Inc). Pelleted vesicles were resuspended in 20 ml of 50 mM HEPES
317 (pH 6.8) and filtered through 0.22 μm pore size filters. Vesicles were again pelleted as

318 described above and finally resuspended in 50 mM HEPES, pH 6.8, except for vesicle
319 preparations used for electrochemistry which were suspended in 100 mM MES, 100 mM
320 KCl, pH 6.8. Extracellular DNA, flagella, and pili can all be co-purified. Protocol was
321 adapted from Perez-Cruz et al(65).

322 **Cryoelectron tomography** Vesicle samples were diluted to a protein concentration of
323 0.4 mg/mL and applied to glow-discharged, X-thick carbon-coated, R2/2, 200 mesh
324 copper Quantifoil grid (Quantifoil Micro Tools) using a Vitrobot chamber (FEI). Grids were
325 automatically plunge frozen and saved for subsequent imaging. No fixative was used.
326 Images were collected on an FEI Krios transmission electron microscope equipped with
327 a K2 Summit counting electron-detector camera (Gatan). Data were collected using
328 customized scripts in SerialEM(66), with each tilt series ranging from −60° to 60° in 3°
329 increments, an underfocus of ∼1-5 µm, and a cumulative electron dose of 121 e/A^2 for
330 each individual tilt series. Tomograms were reconstructed using a combination of
331 ctffind4(67) and the IMOD software package(68).

332
333 **Dynamic Light Scattering** Distributions of vesicle diameters were measured with Wyatt
334 Technology's Möbiuζ dynamic light scattering instrument with DYNAMICS software for
335 data collection and analysis. Data was collected using a 0-50 mW laser at 830 nm. The
336 scattered photons were detected at 90˚. Measurements were recorded from 11 biological
337 replicates for WT OMVs, and 9 replicates for Δ*bdpA* OMVs. Mobius software analyzed
338 the population of particles to generate a table with binned diameters and the percentage
339 of particles at each diameter. In order to compute the average vesicle size from each
340 sample, a weighted average was computed so that diameter bins that had the most
341 number of vesicles would be accurately represented in the final average weight of the

342 population. The product of each diameter is multiplied by its percentage in the population,
343 these products are added together for each sample, divided by the sum of weights. The
344 weighted diameters per replicate were then averaged for each genotype. Statistical
345 significance was determined by Student's *t*-test, and error bars represent standard
346 deviation.

347 **Electrochemistry** CHA Industries Mark 40 e-beam and thermal evaporator was used to
348 deposit a 5 nm Ti adhesion layer and then a 100 nm Au layer onto cleaned glass
349 coverslips (43mm x 50mm #1 Thermo Scientific Gold Seal Cover Glass, Portsmouth NH,
350 USA). Self-assembled monolayers were formed by incubated the gold coverslip in a
351 solution of 1mM 6-mercaptohexanoic acid in 200 proof ethanol for at least 2 hours.
352 Electrode was then rinsed several time in ethanol followed by several rinses in milliQ
353 water. The SAMs layer was then activated by incubation in 100 mM N-(3-
354 Dimethylaminopropyl)-N′-ethylcarbodiimide hydrochloride and 25 mM N-
355 hydroxysuccinimide, pH 4, for 30 minutes. A sample of outer membrane vesicles was
356 deposited on the surface of the electrode and incubated at room temperature overnight
357 in a humid environment. Cyclic voltammetry was performed in a 50 mL three-electrode
358 half-cell completed with a platinum counter electrode, and a 1 M KCl Ag/AgCl reference
359 electrode electrical controlled by a Gamry 600 potentiostat (Gamry, Warminster, PA).
360 The whole experiment was completed in an anaerobic chamber with 95% nitrogen, 5%
361 hydrogen atmosphere.

362 **Proteomics** Vesicle samples were prepared as described above. *S. oneidensis* outer
363 membrane (OM) was purified via the Sarkosyl method described by Brown et al.(69). A
364 50 mL overnight culture of cells was harvested by centrifugation at 10,000 × g for 10 min.
365 The cell pellet suspended in 20 mL of 20 mM ice-cold sodium phosphate (pH 7.5) and
366 passed four times through a French Press (12000 lb/in^2). The lysate was centrifuged at
367 5,000 × g for 30 min to remove unbroken cells. The remaining supernatant was
368 centrifuged at 45,000 × g for 1 h to pellet membranes. Crude membranes were
369 suspended in 20 mL 0.5% Sarkosyl in 20 mM sodium phosphate and shaken horizontally
370 at 200 rpm for 30 min at room temperature. The crude membrane sample was centrifuged
371 at 45,000 × g for 1 h to pellet the OM. The pellet of OM was washed in ice-cold sodium
372 phosphate and recentrifuged.

373 To prepare for mass spectrometry samples were treated sequentially with urea,
374 TCEP, iodoactinamide, lysl endopeptidase, trypsin, and formic acid. Peptides were then
375 desalted by HPLC with a Microm Bioresources C8 peptide macrotrap (3x8mm). The
376 digested samples were subjected to LC-MS/MS analysis on a nanoflow LC system,
377 EASY-nLC 1200, (Thermo Fisher Scientific) coupled to a QExactive HF Orbitrap mass
378 spectrometer (Thermo Fisher Scientific, Bremen, Germany) equipped with a Nanospray
379 Flex ion source. Samples were directly loaded onto a PicoFrit column (New Objective,
380 Woburn, MA) packed in house with ReproSil-Pur C18AQ 1.9 um resin (120A° pore size,
381 Dr. Maisch, Ammerbuch, Germany). The 20 cm x 50 µm ID column was heated to 60°
382 C. The peptides were separated with a 120 min gradient at a flow rate of 220 nL/min.
383 The gradient was as follows: 2–6% Solvent B (7.5 min), 6-25% B (82.5 min), and 25-40%
384 B (30 min) and to 100% B (9min). Solvent A consisted of 97.8% H2O, 2% acetonitrile,

385 and 0.2% formic acid and solvent B consisted of 19.8% H2O, 80% ACN, and 0.2% formic
386 acid. The QExactive HF Orbitrap was operated in data dependent mode with the Tune
387 (version 2.7 SP1build 2659) instrument control software. Spray voltage was set to 2.5
388 kV, S-lens RF level at 50, and heated capillary at 275 °C. Full scan resolution was set to
389 60,000 at m/z 200. Full scan target was 3 × 106 with a maximum injection time of 15 ms.
390 Mass range was set to 300−1650 m/z. For data dependent MS2 scans the loop count
391 was 12, target value was set at 1 × 105, and intensity threshold was kept at 1 × 105.
392 Isolation width was set at 1.2 m/z and a fixed first mass of 100 was used. Normalized
393 collision energy was set at 28. Peptide match was set to off, and isotope exclusion was
394 on. Data acquisition was controlled by Xcalibur (4.0.27.13) and all data was acquired in
395 profile mode.

396 **Bioinformatics** Putative BAR domain SO_1507 (BdpA) was identified in search of
397 annotation terms of *S. oneidensis* MR-1. The conserved domain database (CDD-
398 search)(NCBI) was accessed to identify the position-specific scoring matrix (PSSM) of
399 the specific region of SO_1507 that represented the BAR domain (amino acid residues
400 at positions 276-421). The domain prediction matched to BAR superfamily cl12013 and
401 specifically to the family member BAR cd07307. LOGICOIL multi-state coiled-coil
402 oligomeric state prediction was used to predict the presence of coiled-coils within
403 BdpA(47). SignalP 6.1 was used to detect the presence of the signal peptide and cellular
404 localization of BdpA(70). I-TASSER protein structure prediction(51) was used to generate
405 a predicted model of the BAR domain region of BdpA. Alignment of the predicted BdpA
406 BAR domain structure model to the structure of Hof1p was performed in the PyMOL
407 Molecular Graphics System, Version 2.0 (Schrödinger, LLC).

408 A PSI-BLAST(71) search against the NCBI nr database was performed using the
409 BdpA BAR sequence as the initial search seed to determine how prevalent the BdpA BAR
410 domain is in related species. Conserved BdpA orthologs were annotated as hypothetical
411 proteins in all of the species identified. In the initial round, 24 proteins were found from
412 other organisms identified as *Shewanella* with a high conservation among the proteins
413 and another 28 proteins were found in more distant bacteria species that had similarity of
414 65% to 44%. A second iteration identified a few proteins much more distantly related from
415 bacterial species and then proteins from eukaryote phylum *Arthropoda* that were
416 annotated as being centrosomal proteins. All of the found proteins from bacterial species
417 were hypothetical proteins with no known function. Only five of the proteins from the
418 search returned hits to the PSSM of the BAR cd07307. The identity among the proteins
419 was very high and examination of the proteins suggests that a functional form similar to
420 the BAR domain would result for all the found proteins. Overall, this places BdpA as a
421 protein that just barely meets criteria via PSSM models to be assigned as matching the
422 BAR domain while the rest of the proteins found have enough differences to fail to match
423 the BAR model while still being very similar to BdpA. An attempt was made to build up a
424 HMM (Hidden Markov Model) using hmmer(72) to use for searching for other proteins
425 that might match, but as with the PSI-BLAST search, only the proteins that formed the
426 model returned as good matches. There appears to be a tight clade of very similar
427 proteins with very little differentiation in the sequence. This indicates that while sequence
428 homology between BdpA and the existing BAR domain consensus sequence predicted
429 the BAR domain region in BdpA using hmmer or NCBI tools, the sequence conservation
430 is at the cusp of a positive hit by the HMM since other closely related (>90% homology)

431 BdpA orthologs were not predicted to contain a BAR domain by this method. The most
432 homologous eukaryotic protein to BdpA (27%) is a putative centrosomal protein in
433 *Vollenhovia emeryi* (accession #: XP_011868153) that is predicted to contain an amino
434 terminal C2 membrane binding domain and a carboxy-terminal SMC domain within a
435 coiled-coil region. Despite CDD search failing to predict the presence of a BAR domain
436 in this protein, it does not preclude the presence of one, pending an updated BAR Pfam
437 HMM. Alignments and phylogenies were constructed in MEGA 7. MUSCLE was used to
438 align protein sequences, and Maximum Likelihood phylogenies were inferred using the
439 Le-Gascuel (LG+G) substitution matrix(73). Initial trees for the heuristic search were
440 obtained automatically by applying Neighbor-Join and BioNJ algorithms to a matrix of
441 pairwise distances estimated using a JTT model, and then selecting the topology with
442 superior log likelihood value. A discrete Gamma distribution was used to model
443 evolutionary rate differences among sites as indicated in figure legends. All positions with
444 less than 85% site coverage were eliminated.

445 **Confocal microscopy** For *in vivo* imaging of intrinsic outer membrane extension
446 production, *S. oneidensis* MR-1 strains were grown in LB media overnight, washed twice
447 with SDM, and diluted to an OD_{600} of 0.05 in 1 mL of SDM with appropriate antibiotics.
448 Prior to pipetting, ~1cm of the pipette tip was trimmed to minimize shear forces during
449 transfer. 100 µL of each culture was labeled with 1 µL 1M FM 4-64 to visualize the cell
450 membranes. After staining, 10 µL of the labeled cell suspension was gently pipetted onto
451 22 x 22 mm No.1 cover glass (VWR) and sealed onto glass slides with clear acrylic nail
452 polish for confocal imaging or onto Lab-Tek chambered #1 cover glass (Thermo Fischer
453 Scientific)(for widefield fluorescence). On average, intrinsic membrane extension

454 formation could be observed starting after 45 minutes sealed onto cover glass. For
455 planktonic OME production from BdpA induction in trans, diluted cells (in either SDM for
456 *S. oneidensis*, BB for *M. atlanticus*, or LB for *E. coli*) were induced with 12.5 μM DAPG
457 for 1 hour at 30˚C with 200 RPM shaking agitation. Cells were labeled with FM 4-64 and
458 sealed onto glass slides as before. Induced OMEs were imaged immediately after
459 mounting onto slides.

460 Confocal images were taken by a Zeiss LSM 800 confocal microscope with a Plan-
461 Apochromat 63x/1.4 numerical aperture oil immersion M27 objective. FM 4-64
462 fluorescence was excited at 506 nm: 0.20% laser power. Emission spectra was detected
463 from 592-700 nm using the LSM 800 GaAsP-Pmt2 detector. To capture the dynamics of
464 the OMEs, images were collected over the designated length of time between 0.27 – 0.63
465 seconds per frame. Single frame time series images were collected of either a 50.71 μm
466 by 50.71 μm (2x zoom) or a 20.28 μm by 20.28 μm (5x zoom) field of view. Widefield
467 fluorescence images were taken using a LED-Module 511 nm light source at 74.2%
468 intensity with 583-600 nm filters and a 91 He CFP/YFP/mCherry reflector. Excitation and
469 emission spectra were 506 nm and 751 nm, respectively. Images were collected using a
470 Hamamatsu camera with a 250 ms exposure time. Images were recorded using the Zeiss
471 Zen software (Carl Zeiss Microscopy, LLC, Thornwood, NY, USA). Frequency of OMEs
472 was calculated from 3 biological replicates of each strain from at least 5 fields of view
473 selected at random (2444 cells from WT, 4378 from Δ*bdpA*, and 3354 from Δ*bdpA* p452-
474 *bdpA*). OMEs were counted per cell per field of view from a 20 second video if a
475 membrane extension was observed extending from the cell over that timeframe.
476 Statistical significance was determined by two-tailed Student's *t*-test.

477 **Perfusion flow microscopy** For OME statistics comparing *S. oneidensis* strains MR-1
478 and Δ*bdpA,* cells were pre-grown aerobically from frozen (-80°C) stock in 10 mL of Luria-
479 Bertani (LB) broth (supplemented with 50 µg/mL Kanamycin for strains with plasmid) in a
480 125-mL flask overnight at 30°C and 225 rpm. The next day, the stationary phase (OD_{600}
481 3.0 – 3.3) preculture was used to inoculate 1:100 into 10 mL of fresh LB medium in a 125-
482 mL flask. After ~6 hours at 30°C and 225 rpm, when the OD_{600} was 2.4 (late log phase),
483 5 mL of cells were collected by centrifugation at 4226 x *g* for 5 min and washed twice in
484 defined medium. The perfusion chamber, microscope, and flow medium described
485 previously(7, 29, 30) were used for all perfusion flow OME statistics experiments. During
486 each 5 hour imaging experiment, the perfusion chamber was first filled with this flow
487 medium, then <1 mL of washed cells were slowly injected for a surface density of ~100-
488 300 cells per 112 x 112 µm field of view on a Nikon Eclipse Ti-E inverted microscope with
489 the NIS-Elements AR software. Cells were allowed to attach for 5-15 minutes on the
490 coverslip before perfusion flow was resumed at a volumetric flow rate of 6.25 ± 0.1 µL/s.
491 Cells and OMEs were visualized with the red membrane stain FM 4-64FX in the flow
492 medium (0.25 µg/mL of flow medium). A total of 1,831 wild type and 2,265 Δ*bdpA* cells
493 were used for extension and vesicle quantification. Experiments were performed from
494 three individual biological replicates for each strain, and statistical significance was
495 determined by two-tailed χ^2 test.

496 **Cryo transmission electron microscopy**

497 *Shewanella* strains were streaked onto LB plates with or without kanamycin and allowed
498 to incubate 3 days on a benchtop. The night before freezing, individual colonies were
499 inoculated into 3 ml LB +/- kanamycin and incubated at 30 °C overnight with 200 rpm

500 shaking. The following morning optical densities of the cultures were measured at
501 600nm and adjusted to a final OD_{600} of 1. Cells were pelleted at 8,000 rpm for three
502 minutes for buffer exchange/washes. For the Δ*bdpA* p452-*bdpA* transformed cells, 12.5
503 μM DAPG was added. A freshly glow discharged 200 mesh copper grid with R2/1
504 Quantifoil carbon film was placed into a concavity slide. Approximately 150 μl of a 1:10
505 dilution of the cell suspensions, with or without the inducer, was added to cover the grid.
506 A glass coverslip was then lowered onto the concavity to exclude air bubbles. The
507 edges of the coverslip were then sealed with nail polish to prevent media evaporation.
508 The slide assembly was then incubated in a 30 °C incubator for 1.5 to 3 hours.
509 Immediately prior to plunge freezing, the top coverslip was removed by scoring the nail
510 polish with a razor blade. TEM grids with cells were gently retrieved with forceps and
511 loaded into a Leica grid plunge for automated blotting and plunging into LN_2-cooled
512 liquid ethane. Vitrified grids were transferred to a LN_2 storage dewar. Imaging of frozen
513 samples was performed on either a Titan (ThermoFisher Scientific) microscope
514 equipped with a Gatan Ultrascan camera and operating at 300 kV or a Talos
515 (ThermoFisher Scientific) equipped with a Ceta camera and operating at 200 kV.
516 Images were acquired at 10,000x to 20,000x magnification and were adjusted by
517 bandpass filtering. Unfixed OMEs were sorted based on appearance into 4 categories.
518 Tubules were narrow OMEs with relatively uniform or slight symmetric curvature.
519 Narrow chains were recorded as OMEs with a narrow, consistent diameter and
520 symmetric curvature at constriction points. Irregular chains were classified as OMEs
521 without a consistent diameter throughout the length of the OME and asymmetric
522 curvature on either side of the extension. Blebs \ bulges were outer membrane

523 structures that did not resemble OMEs but still extended from the cell membrane
524 surface. Phenotypes were documented from observations of 31 WT, 13 Δ*bdpA*, and 3
525 Δ*bdpA* p452-*bdpA* OMEs over three separate biological replicates, with two technical
526 replicates of each strain per biological replicate.

527

528 **Acknowledgements**

529 We thank Dr. Jeffery Gralnick for helpful discussions and advice; Dr. Adam Meyer
530 and Dr. Chris Voigt for the DAPG-inducible Marionette promoter; Dr. Annie Moradian and
531 Dr. Mike Sweredoski and the California Institute of Technology Proteome Exploration Lab
532 for useful discussions on the preparation and analysis of proteomics data. Some of the
533 cryo-TEM work was done in the Beckman Institute Resource Center for Transmission
534 Electron Microscopy at Caltech. This work was supported by the United States
535 Department of Defense Synthetic Biology for Military Environments (SBME) Applied
536 Research for the Advancement of Science and Technology Priorities (ARAP) program.
537 Work in ME-N's lab was supported by the U.S. Office of Naval Research Multidisciplinary
538 University Research Initiative Grant No. N00014-18-1-2632. LAZ was partially supported
539 by the National Science Foundation grant DEB-1542527. SX was supported by the
540 Division of Chemical Sciences, Geosciences, and Biosciences, Office of Basic Energy
541 Sciences of the U.S. Department of Energy through grant DE-FG02-13ER16415. Work
542 in GJJ's lab was supported by the National Institute of Health (GM122588 to GJJ).

543 **Author Contributions**

544 DP and LZ conceived the study independently then combined projects when
545 complementary data on BdpA was discovered. LZ purified OMVs, prepared samples for
546 LC MS-MS, and performed DLS measurements. LZ and SX made electrochemical
547 measurements and analysis. DP conducted BdpA domain prediction and validation
548 analysis, generated the p452-*bdpA* plasmid, Δ*bdpA* and p452-*bdpA* strains. DP and GC
549 conducted fluorescence imaging experiments, and DP, LZ, and GC analyzed the data.
550 LB adapted the Marionette sensor (P_{phlF}-YFP) into pBBR1-mcs2. LZ and LAM performed
551 cryo-TEM of OMVs. GC and LZ analyzed perfusion flow system data. CH, DP, and LD
552 performed cryo-TEM experiments of OMEs and image processing / analysis. DP and AM
553 generated phylogenetic data, and DP, AM, and BE analyzed the data. DP, LZ, CM, GC,
554 AM, LAM, BE, GJJ, LD, MEN, and SG provided data interpretation. DP, LZ, MEN, and
555 SG wrote the manuscript, with input from all coauthors.

556

557 ## References

558 1. Carman PJ & Dominguez R (2018) BAR domain proteins-a linkage between cellular membranes,
559 signaling pathways, and the actin cytoskeleton. *Biophys Rev* 10(6):1587-1604.
560 2. Schoneberg J*, et al.* (2017) Lipid-mediated PX-BAR domain recruitment couples local membrane
561 constriction to endocytic vesicle fission. *Nat Commun* 8:15873.
562 3. van Weering JR & Cullen PJ (2014) Membrane-associated cargo recycling by tubule-based
563 endosomal sorting. *Semin Cell Dev Biol* 31:40-47.
564 4. Knaevelsrud H*, et al.* (2013) Membrane remodeling by the PX-BAR protein SNX18 promotes
565 autophagosome formation. *J Cell Biol* 202(2):331-349.
566 5. Mim C & Unger VM (2012) Membrane curvature and its generation by BAR proteins. *Trends*
567 *Biochem Sci* 37(12):526-533.
568 6. Rao Y & Haucke V (2011) Membrane shaping by the Bin/amphiphysin/Rvs (BAR) domain protein
569 superfamily. *Cell Mol Life Sci* 68(24):3983-3993.
570 7. Chong GW, Pirbadian S, & El-Naggar MY (2019) Surface-Induced Formation and Redox-
571 Dependent Staining of Outer Membrane Extensions in Shewanella oneidensis MR-1. *Frontiers in*
572 *Energy Research* 7.
573 8. Fischer T*, et al.* (2019) Biopearling of Interconnected Outer Membrane Vesicle Chains by a
574 Marine Flavobacterium. *Appl Environ Microbiol* 85(19).
575 9. Toyofuku M, Nomura N, & Eberl L (2018) Types and origins of bacterial membrane vesicles.
576 *Nature Reviews Microbiology*.
577 10. Hampton CM*, et al.* (2017) The Opportunistic Pathogen Vibrio vulnificus Produces Outer
578 Membrane Vesicles in a Spatially Distinct Manner Related to Capsular Polysaccharide. *Front*
579 *Microbiol* 8:2177.
580 11. Kim EY, Tyndall ER, Huang KC, Tian F, & Ramamurthi KS (2017) Dash-and-Recruit Mechanism
581 Drives Membrane Curvature Recognition by the Small Bacterial Protein SpoVM. *Cell Syst*
582 5(5):518-526 e513.
583 12. Cornejo E, Subramanian P, Li Z, Jensen GJ, & Komeili A (2016) Dynamic Remodeling of the
584 Magnetosome Membrane Is Triggered by the Initiation of Biomineralization. *MBio* 7(1):e01898-
585 01815.
586 13. Bohuszewicz O, Liu J, & Low HH (2016) Membrane remodelling in bacteria. *J Struct Biol* 196(1):3-
587 14.
588 14. Remis JP*, et al.* (2014) Bacterial social networks: structure and composition of Myxococcus
589 xanthus outer membrane vesicle chains. *Environ Microbiol* 16(2):598-610.
590 15. Wei X, Vassallo CN, Pathak DT, & Wall D (2014) Myxobacteria produce outer membrane-
591 enclosed tubes in unstructured environments. *J Bacteriol* 196(10):1807-1814.
592 16. Low HH, Sachse C, Amos LA, & Lowe J (2009) Structure of a bacterial dynamin-like protein lipid
593 tube provides a mechanism for assembly and membrane curving. *Cell* 139(7):1342-1352.
594 17. Peter BJ*, et al.* (2004) BAR domains as sensors of membrane curvature: the amphiphysin BAR
595 structure. *Science* 303(5657):495-499.
596 18. Frost A, De Camilli P, & Unger VM (2007) F-BAR proteins join the BAR family fold. *Structure*
597 15(7):751-753.
598 19. Shimada A*, et al.* (2007) Curved EFC/F-BAR-domain dimers are joined end to end into a filament
599 for membrane invagination in endocytosis. *Cell* 129(4):761-772.

600 20. Weissenhorn W (2005) Crystal structure of the endophilin-A1 BAR domain. *J Mol Biol*
601 351(3):653-661.
602 21. Drin G & Antonny B (2010) Amphipathic helices and membrane curvature. *FEBS Lett*
603 584(9):1840-1847.
604 22. Seet LF & Hong W (2006) The Phox (PX) domain proteins and membrane traffic. *Biochim Biophys*
605 *Acta* 1761(8):878-896.
606 23. Itoh T & De Camilli P (2006) BAR, F-BAR (EFC) and ENTH/ANTH domains in the regulation of
607 membrane-cytosol interfaces and membrane curvature. *Biochim Biophys Acta* 1761(8):897-912.
608 24. Simunovic M, Voth GA, Callan-Jones A, & Bassereau P (2015) When Physics Takes Over: BAR
609 Proteins and Membrane Curvature. *Trends Cell Biol* 25(12):780-792.
610 25. Mim C*, et al.* (2012) Structural basis of membrane bending by the N-BAR protein endophilin. *Cell*
611 149(1):137-145.
612 26. Habermann B (2004) The BAR-domain family of proteins: a case of bending and binding? *EMBO*
613 *reports* 5(3):250-255.
614 27. Miki H, Yamaguchi H, Suetsugu S, & Takenawa T (2000) IRSp53 is an essential intermediate
615 between Rac and WAVE in the regulation of membrane ruffling. *Nature* 408(6813):732-735.
616 28. Sampath V, McCaig WD, & Thanassi DG (2018) Amino acid deprivation and central carbon
617 metabolism regulate the production of outer membrane vesicles and tubes by Francisella. *Mol*
618 *Microbiol* 107(4):523-541.
619 29. Subramanian P, Pirbadian S, El-Naggar MY, & Jensen GJ (2018) Ultrastructure of Shewanella
620 oneidensis MR-1 nanowires revealed by electron cryotomography. *Proc Natl Acad Sci U S A*
621 115(14):E3246-E3255.
622 30. Pirbadian S*, et al.* (2014) Shewanella oneidensis MR-1 nanowires are outer membrane and
623 periplasmic extensions of the extracellular electron transport components. *Proc Natl Acad Sci U*
624 *S A* 111(35):12883-12888.
625 31. Gorby YA*, et al.* (2006) Electrically conductive bacterial nanowires produced by Shewanella
626 oneidensis strain MR-1 and other microorganisms. *Proc Natl Acad Sci U S A* 103(30):11358-
627 11363.
628 32. Bhattacharya S*, et al.* (2019) A Ubiquitous Platform for Bacterial Nanotube Biogenesis. *Cell Rep*.
629 33. Dubey GP*, et al.* (2016) Architecture and Characteristics of Bacterial Nanotubes. *Dev Cell*
630 36(4):453-461.
631 34. Dubey GP & Ben-Yehuda S (2011) Intercellular nanotubes mediate bacterial communication. *Cell*
632 144(4):590-600.
633 35. Pande S*, et al.* (2015) Metabolic cross-feeding via intercellular nanotubes among bacteria. *Nat*
634 *Commun* 6:6238.
635 36. Tanaka M, Arakaki A, & Matsunaga T (2010) Identification and functional characterization of
636 liposome tubulation protein from magnetotactic bacteria. *Mol Microbiol* 76(2):480-488.
637 37. Danne L*, et al.* (2017) Membrane Remodeling by a Bacterial Phospholipid-Methylating Enzyme.
638 *MBio* 8(1).
639 38. Danne L*, et al.* (2017) Dissection of membrane-binding and -remodeling regions in two classes of
640 bacterial phospholipid N-methyltransferases. *Biochim Biophys Acta* 1859(12):2279-2288.
641 39. Danne L*, et al.* (2015) Membrane-binding mechanism of a bacterial phospholipid N-
642 methyltransferase. *Mol Microbiol* 95(2):313-331.
643 40. Low HH & Lowe J (2006) A bacterial dynamin-like protein. *Nature* 444(7120):766-769.
644 41. Gorby Y*, et al.* (2008) Redox-reactive membrane vesicles produced by Shewanella. *Geobiology*
645 6(3):232-241.
646 42. Liu X*, et al.* (2019) Bacterial Vesicles Mediate Extracellular Electron Transfer. *Environmental*
647 *Science & Technology Letters*.

648 43. Xu S, Barrozo A, Tender LM, Krylov AI, & El-Naggar MY (2018) Multiheme Cytochrome Mediated
649 Redox Conduction through Shewanella oneidensis MR-1 Cells. *J Am Chem Soc* 140(32):10085-
650 10089.
651 44. Okamoto A, Nakamura R, & Hashimoto K (2011) In-vivo identification of direct electron transfer
652 from Shewanella oneidensis MR-1 to electrodes via outer-membrane OmcA–MtrCAB protein
653 complexes. *Electrochimica Acta* 56(16):5526-5531.
654 45. Cox J*, et al.* (2014) Accurate proteome-wide label-free quantification by delayed normalization
655 and maximal peptide ratio extraction, termed MaxLFQ*. Mol Cell Proteomics* 13(9):2513-2526.
656 46. Hsu VW, Bai M, & Li J (2012) Getting active: protein sorting in endocytic recycling. *Nat Rev Mol*
657 *Cell Biol* 13(5):323-328.
658 47. Vincent TL, Green PJ, & Woolfson DN (2013) LOGICOIL--multi-state prediction of coiled-coil
659 oligomeric state. *Bioinformatics* 29(1):69-76.
660 48. Linkner J*, et al.* (2014) The inverse BAR domain protein IBARa drives membrane remodeling to
661 control osmoregulation, phagocytosis and cytokinesis. *J Cell Sci* 127(Pt 6):1279-1292.
662 49. Cui H*, et al.* (2013) Understanding the role of amphipathic helices in N-BAR domain driven
663 membrane remodeling. *Biophys J* 104(2):404-411.
664 50. Henne WM*, et al.* (2007) Structure and analysis of FCHo2 F-BAR domain: a dimerizing and
665 membrane recruitment module that effects membrane curvature. *Structure* 15(7):839-852.
666 51. Roy A, Kucukural A, & Zhang Y (2010) I-TASSER: a unified platform for automated protein
667 structure and function prediction. *Nat Protoc* 5(4):725-738.
668 52. Moravcevic K*, et al.* (2015) Comparison of Saccharomyces cerevisiae F-BAR domain structures
669 reveals a conserved inositol phosphate binding site. *Structure* 23(2):352-363.
670 53. Pylypenko O, Lundmark R, Rasmuson E, Carlsson SR, & Rak A (2007) The PX-BAR membrane-
671 remodeling unit of sorting nexin 9. *EMBO J* 26(22):4788-4800.
672 54. Vinogradov E, Korenevsky A, & Beveridge TJ (2003) The structure of the rough-type
673 lipopolysaccharide from Shewanella oneidensis MR-1, containing 8-amino-8-deoxy-Kdo and an
674 open-chain form of 2-acetamido-2-deoxy-d-galactose. *Carbohydrate Research* 338(19):1991-
675 1997.
676 55. Meyer AJ, Segall-Shapiro TH, Glassey E, Zhang J, & Voigt CA (2018) Escherichia coli "Marionette"
677 strains with 12 highly optimized small-molecule sensors. *Nat Chem Biol*.
678 56. Mahmood MI, Noguchi H, & Okazaki KI (2019) Curvature induction and sensing of the F-BAR
679 protein Pacsin1 on lipid membranes via molecular dynamics simulations. *Sci Rep* 9(1):14557.
680 57. Wang Q*, et al.* (2009) Molecular mechanism of membrane constriction and tubulation mediated
681 by the F-BAR protein Pacsin/Syndapin. *Proc Natl Acad Sci U S A* 106(31):12700-12705.
682 58. Bird LJ*, et al.* (2018) Development of a Genetic System for Marinobacter atlanticus CP1 (sp.
683 nov.), a Wax Ester Producing Strain Isolated From an Autotrophic Biocathode. *Front Microbiol*
684 9:3176.
685 59. Coursolle D & Gralnick JA (2010) Modularity of the Mtr respiratory pathway of Shewanella
686 oneidensis strain MR-1. *Mol Microbiol* 77(4):995-1008.
687 60. Bird LJ*, et al.* (2019) Engineered living conductive biofilms as functional materials. *MRS*
688 *Communications*:1-13.
689 61. Ayton GS*, et al.* (2009) New insights into BAR domain-induced membrane remodeling. *Biophys J*
690 97(6):1616-1625.
691 62. Simunovic M*, et al.* (2013) Protein-mediated transformation of lipid vesicles into tubular
692 networks. *Biophys J* 105(3):711-719.
693 63. Noguchi H (2016) Membrane tubule formation by banana-shaped proteins with or without
694 transient network structure. *Sci Rep* 6:20935.

695 64. Salzer U, Kostan J, & Djinovic-Carugo K (2017) Deciphering the BAR code of membrane
696 modulators. *Cell Mol Life Sci* 74(13):2413-2438.
697 65. Perez-Cruz C*, et al.* (2013) New type of outer membrane vesicle produced by the Gram-negative
698 bacterium Shewanella vesiculosa M7T: implications for DNA content. *Appl Environ Microbiol*
699 79(6):1874-1881.
700 66. Hagen WJH, Wan W, & Briggs JAG (2017) Implementation of a cryo-electron tomography tilt-
701 scheme optimized for high resolution subtomogram averaging. *J Struct Biol* 197(2):191-198.
702 67. Rohou A & Grigorieff N (2015) CTFFIND4: Fast and accurate defocus estimation from electron
703 micrographs. *J Struct Biol* 192(2):216-221.
704 68. Kremer JR, Mastronarde DN, & McIntosh JR (1996) Computer visualization of three-dimensional
705 image data using IMOD. *J Struct Biol* 116(1):71-76.
706 69. Brown RN, Romine MF, Schepmoes AA, Smith RD, & Lipton MS (2010) Mapping the subcellular
707 proteome of Shewanella oneidensis MR-1 using sarkosyl-based fractionation and LC-MS/MS
708 protein identification. *J Proteome Res* 9(9):4454-4463.
709 70. Nielsen H (2017) Predicting Secretory Proteins with SignalP. *Protein Function Prediction:*
710 *Methods and Protocols*, ed Kihara D (Springer New York, New York, NY), pp 59-73.
711 71. Altschul SF*, et al.* (1997) Gapped BLAST and PSI-BLAST: a new generation of protein database
712 search programs. *Nucleic Acids Res* 25(17):3389-3402.
713 72. Finn RD, Clements J, & Eddy SR (2011) HMMER web server: interactive sequence similarity
714 searching. *Nucleic Acids Res* 39(Web Server issue):W29-37.
715 73. Le SQ & Gascuel O (2008) An improved general amino acid replacement matrix. *Mol Biol Evol*
716 25(7):1307-1320.
717 74. Myers CR & Nealson KH (1988) Bacterial manganese reduction and growth with manganese
718 oxide as the sole electron acceptor. *Science* 240(4857):1319-1321.
719 75. Saltikov CW & Newman DK (2003) Genetic identification of a respiratory arsenate reductase.
720 *Proc Natl Acad Sci U S A* 100(19):10983-10988.
721 76. Kovach ME*, et al.* (1995) Four new derivatives of the broad-host-range cloning vector
722 pBBR1MCS, carrying different antibiotic-resistance cassettes. *Gene* 166(1):175-176.
723 77. Simon R, Priefer U, & Pühler A (1983) A Broad Host Range Mobilization System for In Vivo
724 Genetic Engineering: Transposon Mutagenesis in Gram Negative Bacteria. *Bio/Technology*
725 1(9):784-791.

726

727

728

729

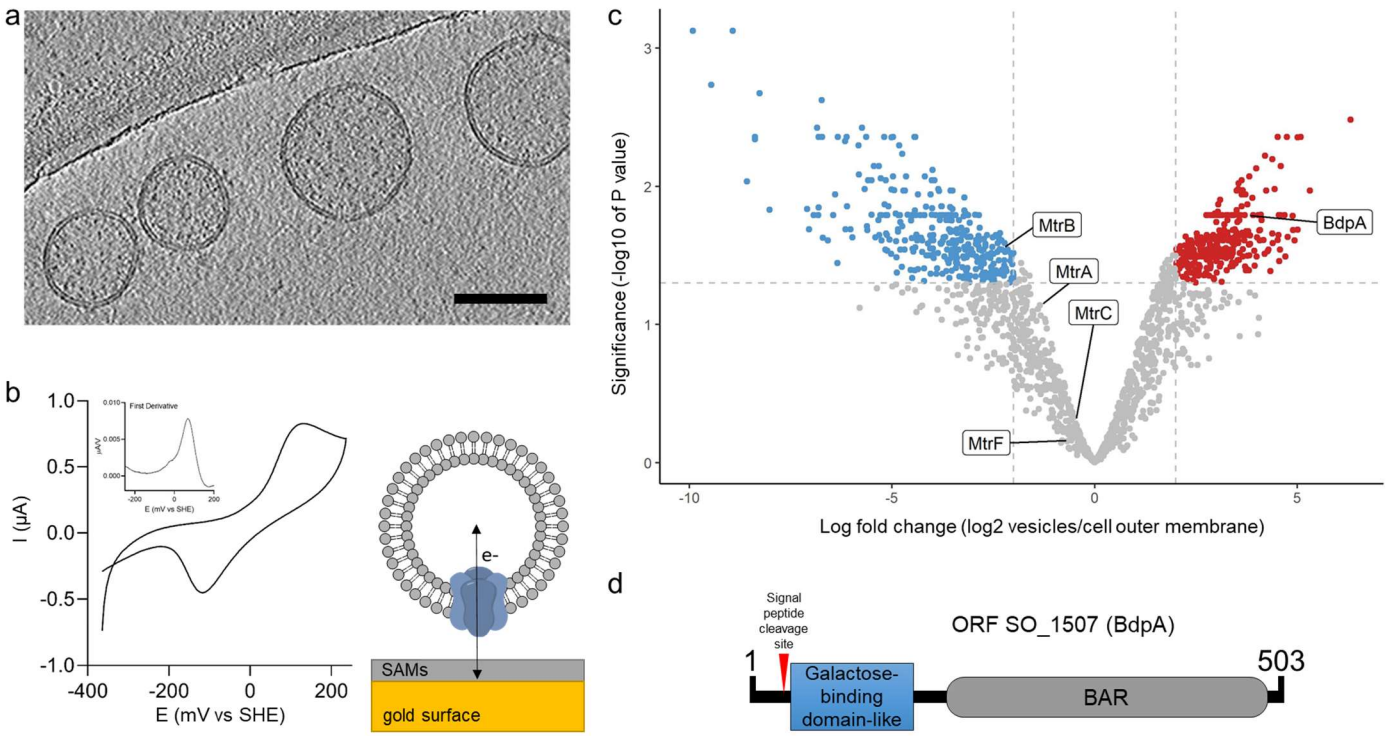

Fig. 1| Redox active vesicles are enriched with BAR domain protein BdpA. a. Cryoelectron tomography image of *S. oneidensis* MR-1 outer membrane vesicles (OMVs) (scale = 200 nm). **b**. Cyclic voltammetry of vesicles adhered to gold electrode via small self-assembled monolayers, as diagramed. Inset shows first derivative of anodic scan. **c**. Volcano plot of vesicle proteome compared to cell-associated outer membrane (red = enriched in vesicles, blue = enriched in cell-associated outer membrane). **d**. Schematic of BdpA domains.

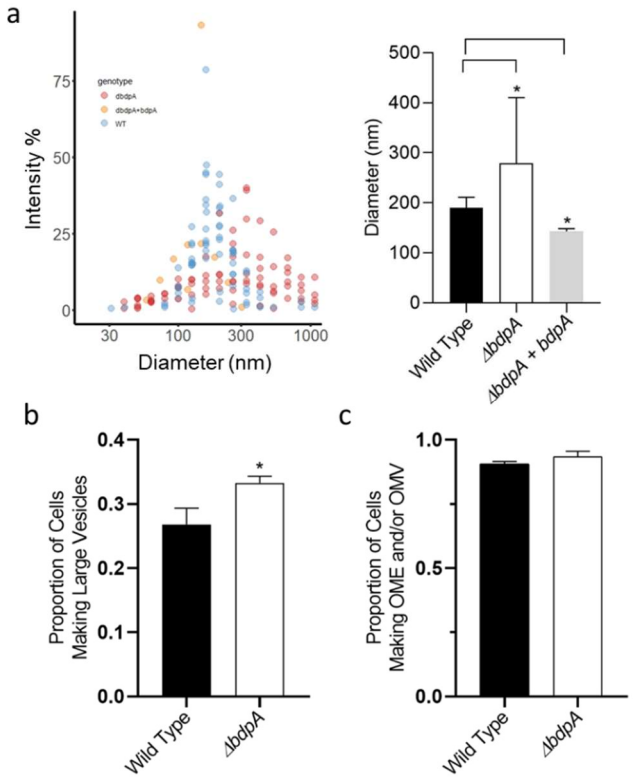

Fig. 2| BdpA is responsible for maintaining vesicle size but does not alter the frequency of OMV or OME formation. a. Dynamic light scattering of OMV size distributions from the deletion strain (red, 9 biological replicates) compared to wild type (blue, 11 biological replicates) and Δ*bdpA* cells expressing *bdpA* from a plasmid (yellow, (left), with weighted averages of OMV diameters (right). Color opacity denotes overlapping data points ($p < 0.05$, *t*-test). **b**. Proportion of cells forming large vesicles (>300 nm diameter) during perfusion flow monitored by time lapse fluorescence imaging ($p < 0.00459$, χ^2 test). **c**. Proportion of cells forming vesicles and extensions relative to the total number of cells observed by fluorescence microscopy during perfusion flow ($p > 0.05$, χ^2 test). Time lapse images were recorded from 3 biological replicates per strain with 5-13 fields of view per replicate. Error bars represent standard deviation.

753

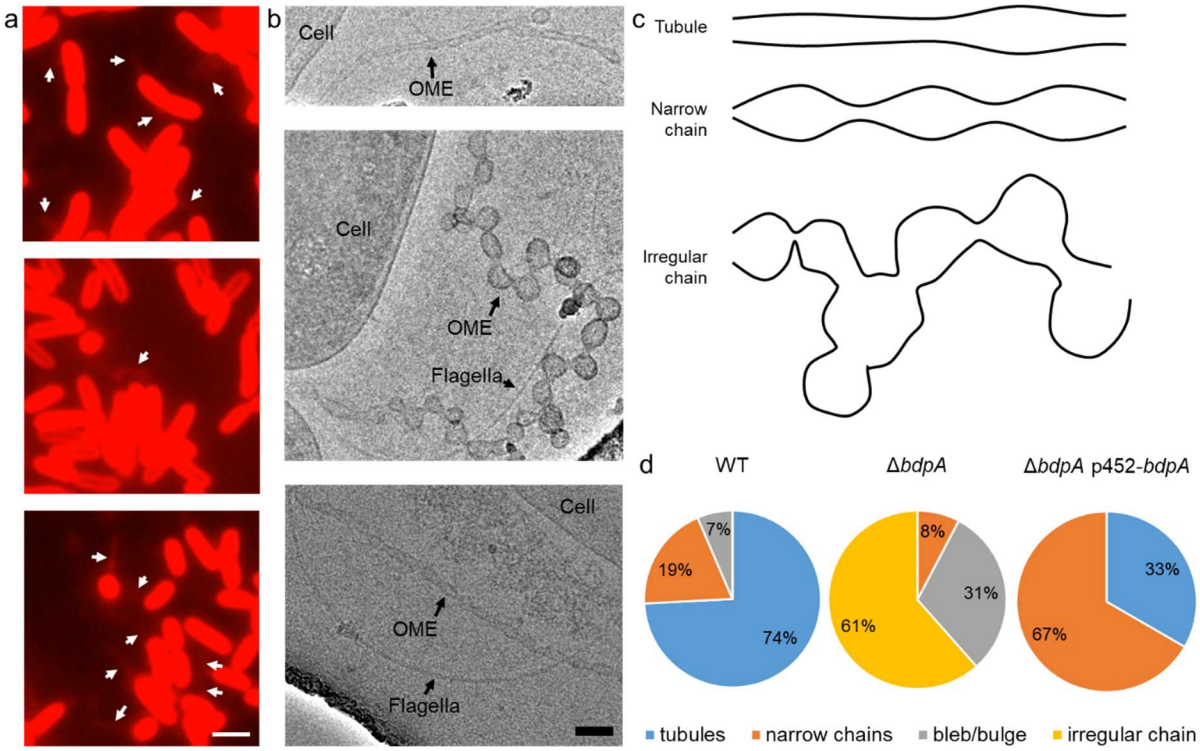

754

755 **Fig. 3| BdpA promotes OME maturation into ordered tubules. a.** Fluorescence
756 images of *S. oneidensis* WT (top), Δ*bdpA* (middle), and Δ*bdpA* p452-*bdpA* with 12.5 μM
757 DAPG (bottom) OMEs. Scale = 2 μm. **b.** Cryo-TEM images of WT (top), Δ*bdpA* (middle),
758 and Δ*bdpA* p452-*bdpA* with 12.5 μM DAPG (bottom) OMEs. Scale = 100 nm. **c.**
759 Representative cartoon of OME phenotypes. **d**. Pie charts show relative frequency of
760 OME phenotypes observed from each strain. Membrane blebs/bulges were defined as
761 non-structured membrane protrusions that did not resemble either of the other OME
762 categories.

763

764

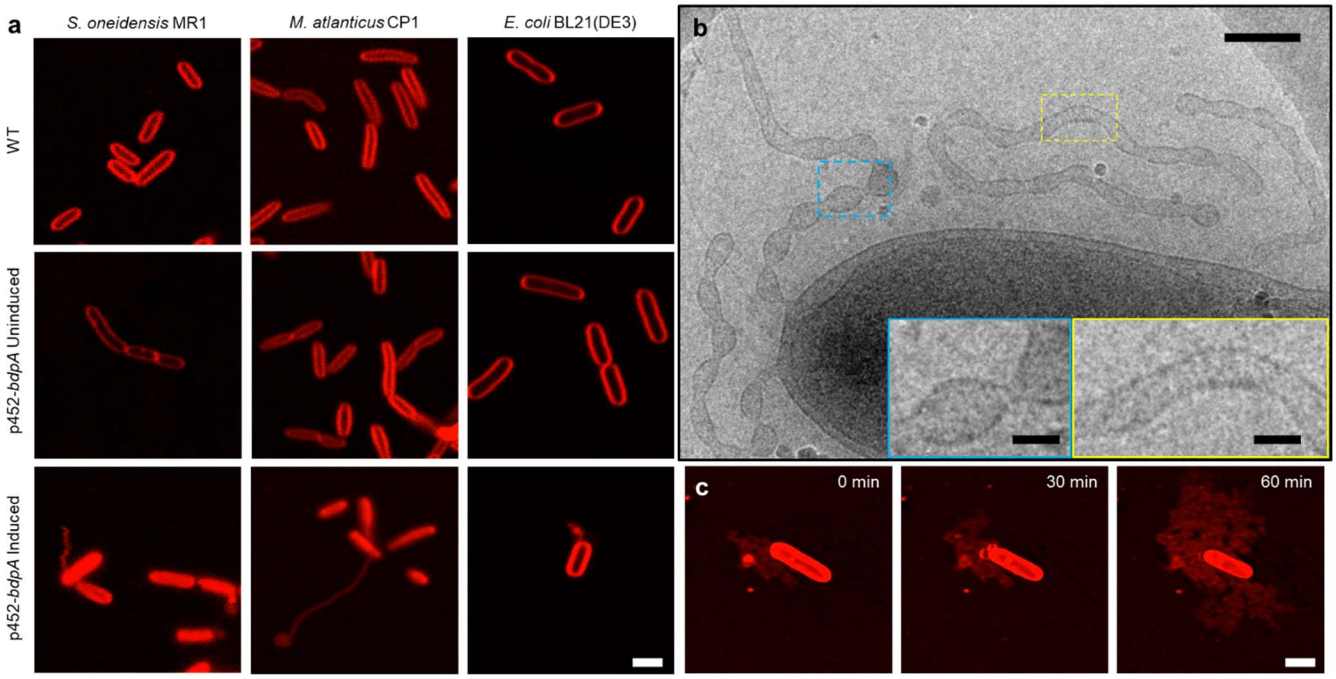

765 **Fig. 4| Heterologous expression of BdpA promotes OME formation.** **a.** Induction of BdpA
766 expression with 12.5 μM DAPG during planktonic, non-attached growth results in OME formation
767 in *S. oneidensis* (left), *M. atlanticus* CP1 (middle), and *E. coli* BL21(DE3) (right). Scale = 2 μm.
768 **b.** Cryo-TEM image of OMEs following planktonic induction of BdpA expression in *S. oneidensis*
769 WT p452-*bdpA* cells. Scale = 200 nm. Insets enlarged to show detail of regularly ordered electron
770 densities at the surface of OME junctions (blue) and tubule regions (yellow). Scale = 50 nm. **c.**
771 OME growth over time at 30 minute intervals of *E. coli* BL21(DE3) expressing BdpA while attached
772 to a glass surface. Scale = 2 μm.

773

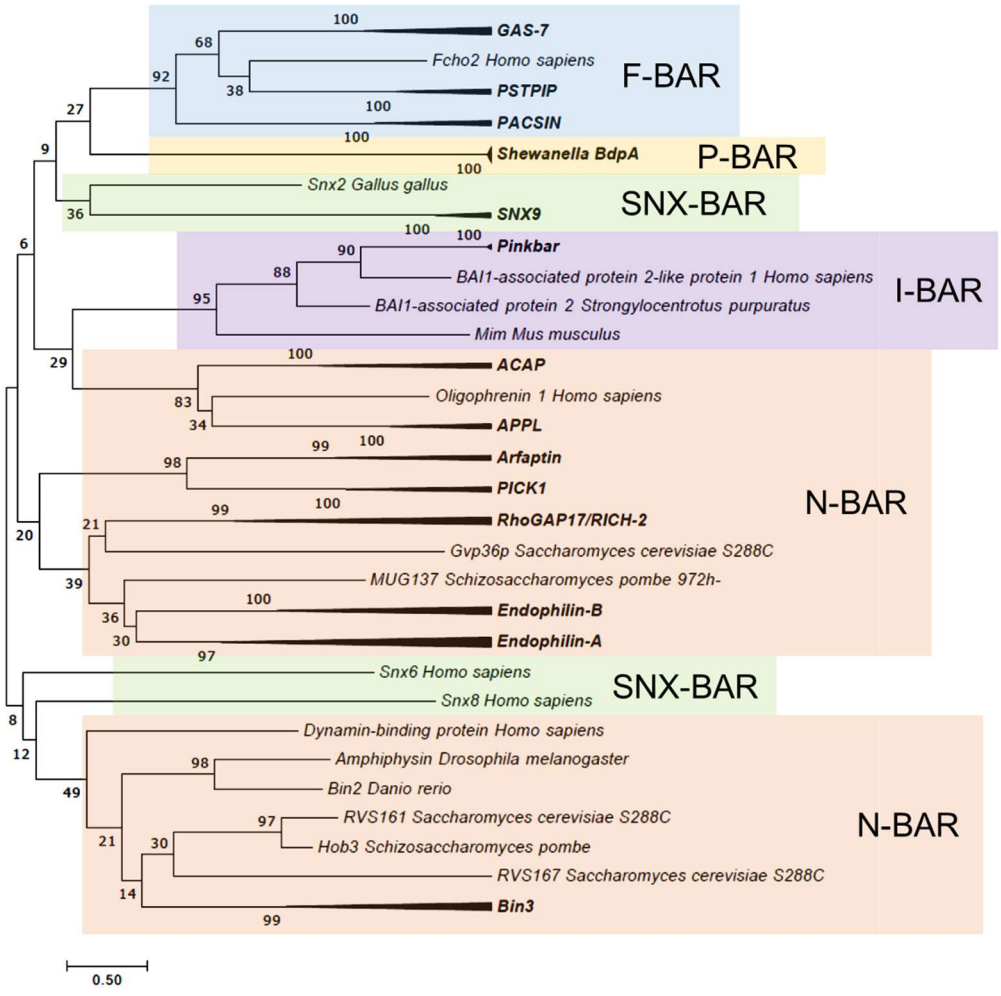

Fig. 5| Comparative phylogenetic analysis of BdpA with prokaryotic homologs and eukaryotic BAR domains. Maximum Likelihood evolutionary histories were inferred from 1000 bootstrap replicates, and the percentage of trees in which the taxa clustered together is shown next to the branches. Arrows indicate multiple branches collapsed to a single node. *S. oneidensis* BdpA and 5 prokaryotic orthologs (WP_011623497 – unclassified *Shewanella*, ESE40074 – *S. decolorationis* S12, WP_039978560 - *S. decolorationis*, KEK29176 – *S. xiamenensis*, and WP_055648003 – *Shewanella sp.* Sh95) predicted by the current BAR domain Pfam HMM to contain a BAR domain aligned with representative BAR domains from various BAR domain subtypes (N-BAR, F-BAR, SNX-BAR, I-BAR) at a total of 196 positions. The Gamma distribution used to model evolutionary rate differences among sites was 12.9598.

787 **Supplemental Table 2**

788

789

Strain, Plasmid, or Primer	Description or relevant genotype	Source or reference
Strains		
Shewanella oneidensis strains		
MR-1	Wild type	[(74)]
Δ*bdpA*	*bdpA* scarless deletion	This study
Marinobacter atlanticus CP1	Wild type	[(58)]
Eschericia coli strains		
BL21(DE3)	OneShot *E. coli* BL21(DE3)	Invitrogen
UQ950	Cloning strain	[(75)]
BW29427 (WM3064)	Conjugation strain	[(75)]
Plasmids		
pBBR1-mcs2	empty vector	[(76)]
pBBJM	Cloning backbone	This study
pSMV3	Suicide vector	[(77)]
pSMV3_1507KO	Contains up and downstream regions of SO_1507	This study
p452-*bdpA*	DAPG inducible *bdpA* vector	This study
Primers		
pAJMF2	TTAACGCGAATTTTAACAAAATATTAACGCcccgcttaacgatcgttggctg	
pAJMR3	AGCGGATAACAATTTCACACAGGAAACAGCTacctcagataaaatatttgc	
pBBRF3	gggctcatgagcaaatattttatctgaggtAGCTGTTTCCTGTGTGAAATTG	
pBBRR2	acccgcgctcagccaacgatcgttaagcgggGCGTTAATATTTTGTTAAAATTCGC	
1507F_insert	ttaatactagagaaagaggggaaatactagATGCGCACCGCTGC	
1507R_insert	gaggcctcttttctggaatttggtaccgagCTACATAAAGGCTTTAGTAAAGGCTT	
BBJMV_reverse	CAGCATTGAGATGACTGCAGCGGTGCGCATctagtatttcccctctttctctagtat	
BBJMV_forward	AAGGAAGCCTTTACTAAAGCCTTTATGTAGctcggtaccaaattccagaaaag	

790 1 Myers, C. R. & Nealson, K. H. Bacterial manganese reduction and growth with manganese oxide as the sole
791 electron acceptor. *Science* **240**, 1319-1321, (1988).
792 2 Bird, L. J. *et al.* Development of a Genetic System for *Marinobacter atlanticus* CP1 (sp. nov.), a Wax Ester
793 Producing Strain Isolated From an Autotrophic Biocathode. *Front Microbiol* **9**, 3176, (2018).
794 3 Saltikov, C. W. & Newman, D. K. Genetic identification of a respiratory arsenate reductase. *Proc Natl Acad*
795 *Sci U S A* **100**, 10983-10988, (2003).
796 4 Kovach, M. E. *et al.* Four new derivatives of the broad-host-range cloning vector pBBR1MCS, carrying
797 different antibiotic-resistance cassettes. *Gene* **166**, 175-176, (1995).
798 5 Simon, R., Priefer, U. & Pühler, A. A Broad Host Range Mobilization System for In Vivo Genetic
799 Engineering: Transposon Mutagenesis in Gram Negative Bacteria. *Bio/Technology* **1**, 784-791, (1983).

800

801 **Supplemental Figure 1**

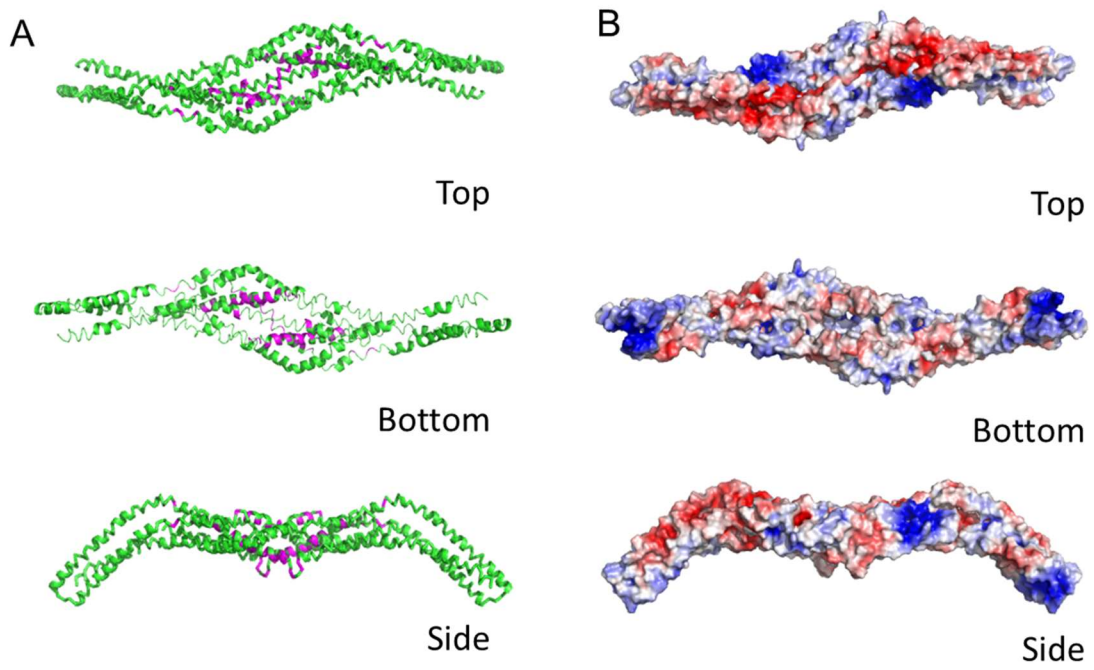

802

803 **Predicted structure of the BAR domain region of BdpA.**
(A) Ribbon diagram of i-TASSER prediction of BdpA structure as a dimeric molecule, residues 175-502. Dimer was modeled from an alignment of BdpA monomers to homodimeric Hof1p (Protein Data Bank [PDB] ID code 4WPE) structures that resulted in closest proximity of putative dimer interface (purple) residues from the initial BAR domain prediction. (B) Surface representation of predicted BdpA homodimer colored according to electrostatic potential. The bottom concave face has an accumulation of distributed positively charged residues (Lys, Arg, His - blue), while the top face has clusters of positive and negatively charged (Glu, Asp - red) residues, within a range of -3.0 to 3.0 V.

804 **Supplemental Figure 2**

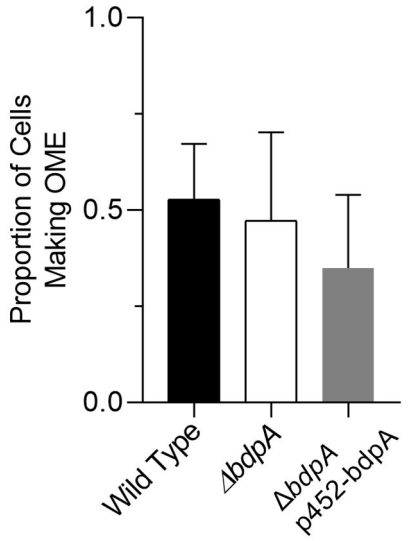

805

806 Proportion of cells making OMEs without perfusion flow at three hours post deposition onto
807 chambered cover glass, measured from five random fields of view from each of three
808 independent cultures per strain.

809

810 **Supplemental Figure 3**

811

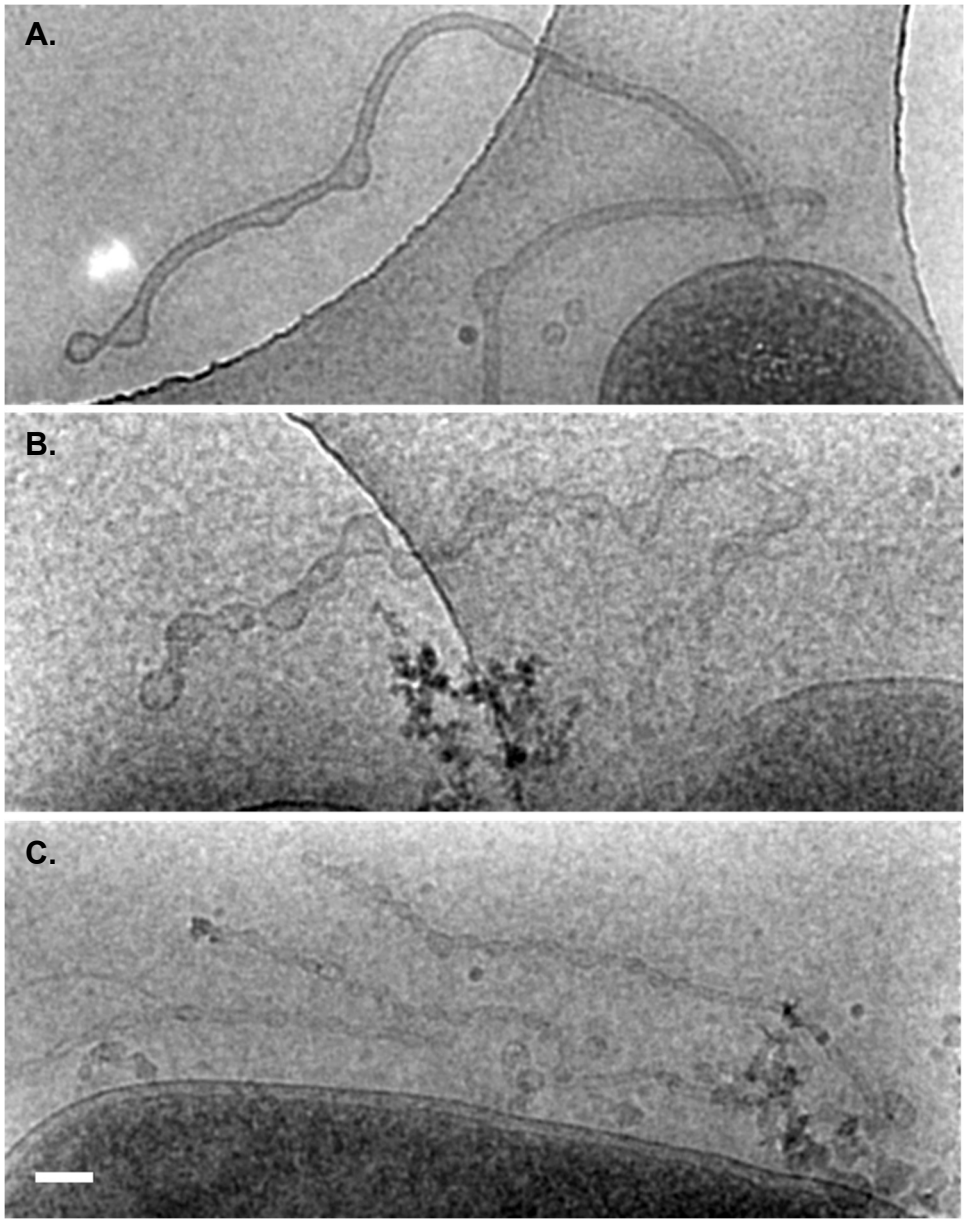

812

813 Cryo-TEM of *S. oneidensis* WT (A), Δ*bdpA* (B), and Δ*bdpA* p452-*bdpA* (C) OMEs at 90 minutes
814 post-surface attachment. Scale = 100 nm.

815

816 **Supplemental Figure 4**

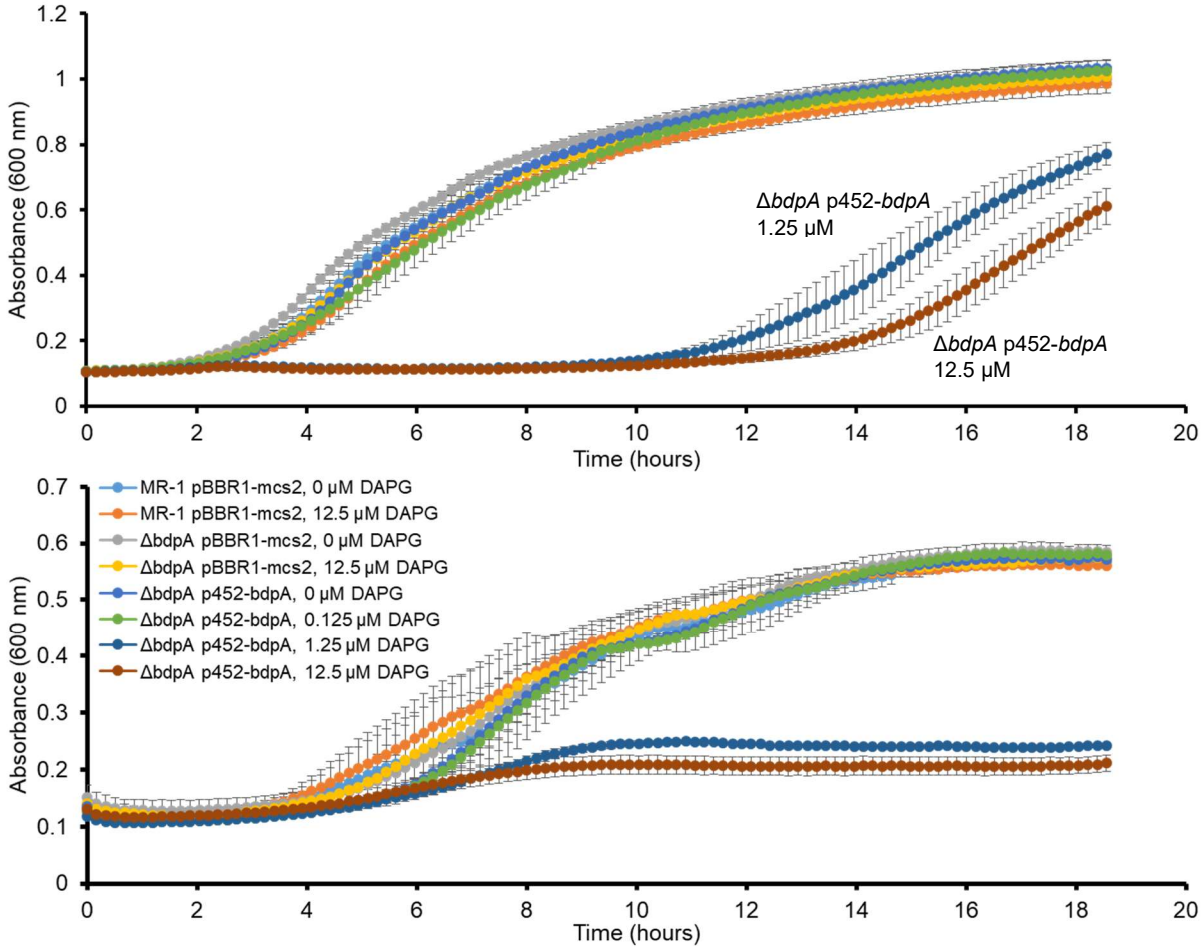

817

818 Growth of *S. oneidensis* strains in LB (top) or *Shewanella* Defined Medium (SDM) (bottom) in
819 response to DAPG exposure and BdpA induction. Error bars are standard deviation of three
820 biological replicates.

821

822 **Supplemental Figure 5**

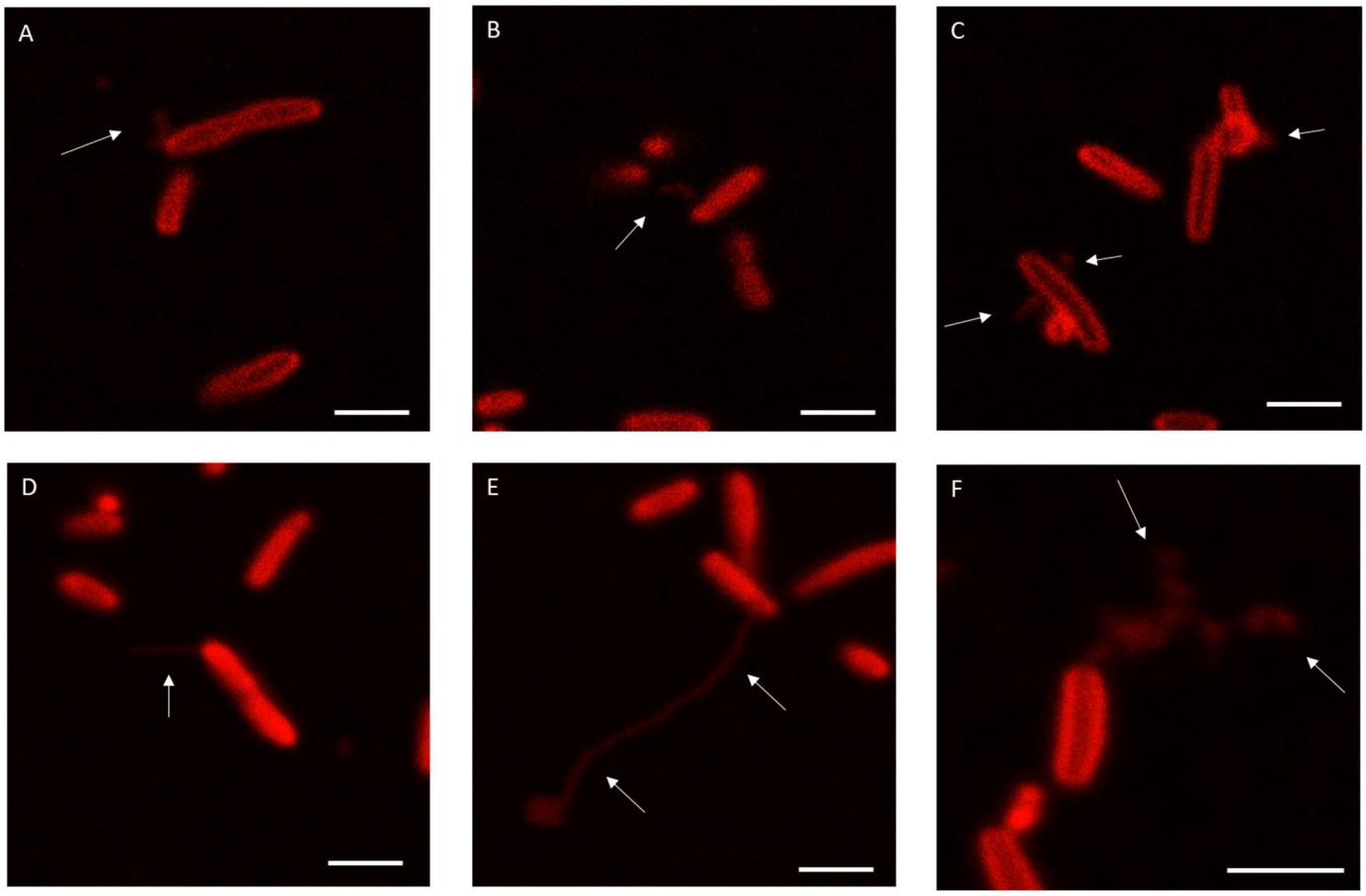

823

824 **Variability in OME phenotypes following BdpA induction in *M. atlanticus* CP1 p452-*bdpA***
825 **cells.** Cells displayed an array of membrane curvature phenotypes, ranging from short OMEs
826 (<2μm, A-C), long OMEs (2-10+ μm, D-F), membrane blebbing (C,F), and branched OME/OMV
827 chains (F). Scale = 2 μm.

828

829 **Supplemental Figure 6**

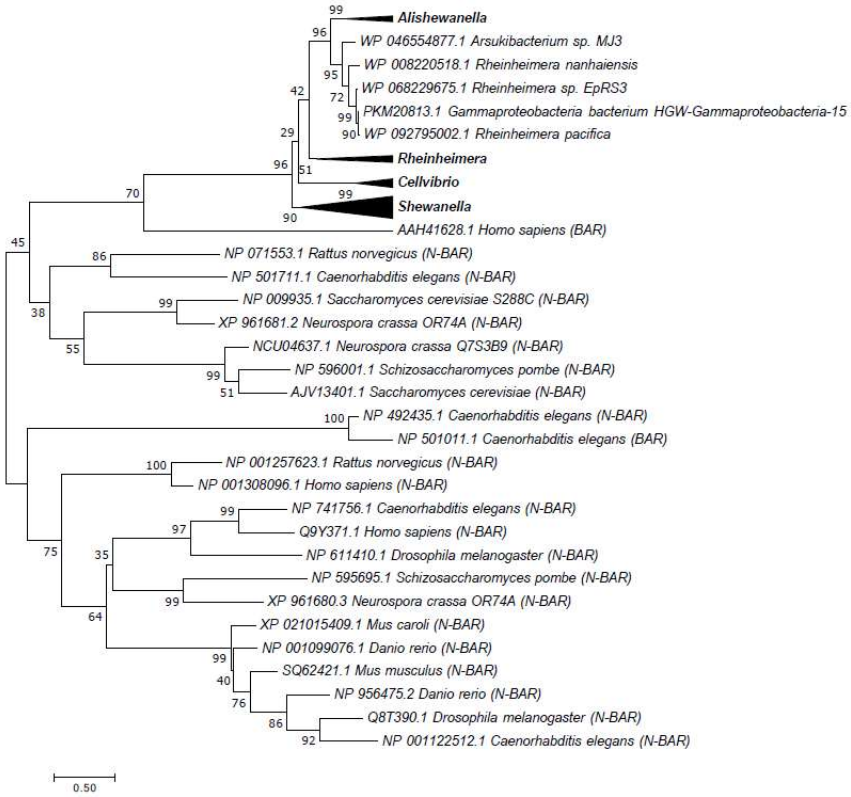

830

831 **BdpA has homologs in other bacterial species.** A phylogenetic tree of the 23 BAR domain
832 sequences that seed the BAR domain HMM predictions, *S. oneidensis* BdpA, and conserved
833 BdpA orthologs in other prokaryotes. The protein regions corresponding to the BdpA BAR
834 domain sequence from the 52 prokaryotic BdpA orthologs were aligned with the 23
835 representative eukaryotic BAR domain-containing proteins used to generate the BAR domain
836 consensus sequence (cd07307) at a total of 222 positions. Maximum Likelihood evolutionary
837 histories were inferred from 1000 bootstrap replicates, and the percentage of trees in which the
838 taxa clustered together is shown next to the branches. The Gamma distribution used to model
839 evolutionary rate differences among sites was 11.9548.

840

841 **Supplementary Video 1** Widefield imaging of *S. oneidensis* WT cells 3h post-
842 deposition onto the surface of a chambered cover glass. Scale = 5 μm.

843

844 **Supplementary Video 2** Widefield imaging of *S. oneidensis* Δ*bdpA* cells 3h post-
845 deposition onto the surface of a chambered cover glass. Scale = 5 μm.

846

847 **Supplementary Video 3** Widefield imaging of *S. oneidensis* Δ*bdpA* p452-*bdpA* cells 3h
848 post-deposition onto the surface of a chambered cover glass. Scale = 5 μm.

849

850 **Supplementary Video 4** Confocal imaging of *S. oneidensis* MR-1 p452-*bdpA* cells after
851 1h planktonic induction of BdpA with 12.5 μM DAPG. Scale = 5 μm.

852